

Published in final edited form as:

*Magn Reson Imaging*. 2014 June ; 32(5): 541–550. doi:10.1016/j.mri.2014.02.002.

## XeNA: An automated ‘open-source’ $^{129}\text{Xe}$ hyperpolarizer for clinical use

Panayiotis Nikolaou<sup>a,b</sup>, Aaron M. Coffey<sup>a,i</sup>, Laura L. Walkup<sup>b,†</sup>, Brogan M. Gust<sup>b</sup>, Nicholas Whiting<sup>c,\*</sup>, Hayley Newton<sup>c</sup>, Iga Muradyan<sup>e</sup>, Mikayel Dabaghyan<sup>e</sup>, Kaili Ranta<sup>d</sup>, Gregory D. Moroz<sup>f</sup>, Matthew S. Rosen<sup>g,h</sup>, Samuel Patz<sup>e</sup>, Michael J. Barlow<sup>c</sup>, Eduard Y. Chekmenev<sup>a,i,j</sup>, and Boyd M. Goodson<sup>b</sup>

<sup>a</sup>Department of Radiology, Vanderbilt University Institute of Imaging Science (VUIIS), Nashville, TN, 37232, United States

<sup>b</sup>Department of Chemistry & Biochemistry, Southern Illinois University, Carbondale, IL

<sup>c</sup>Sir Peter Mansfield Magnetic Resonance Centre, University of Nottingham, Nottingham, NG7 2RD, UK

<sup>d</sup>Department of Physics, Southern Illinois University, Carbondale, IL

<sup>e</sup>Department of Radiology, Brigham & Women’s Hospital and Harvard Medical School, Boston, MA

<sup>f</sup>Graduate School Central Research Shop, Southern Illinois University, Carbondale, IL

<sup>g</sup>MGH/A.A. Martinos Center for Biomedical Imaging, Boston MA

<sup>h</sup>Department of Physics, Harvard University, Cambridge MA

<sup>i</sup>Department of Biomedical Engineering, Vanderbilt University, Nashville, Tennessee, 37235, United States

<sup>j</sup>Department of Biochemistry, Vanderbilt University, Nashville, Tennessee, 37205, United States

### Abstract

Here we provide a full report on the construction, components, and capabilities of our consortium’s “open-source” large-scale (~1 L/hr)  $^{129}\text{Xe}$  hyperpolarizer for clinical, pre-clinical, and materials NMR/MRI (Nikolaou *et al.*, *Proc. Natl. Acad. Sci. USA*, 110, 14150 (2013)). The ‘hyperpolarizer’ is automated and built mostly of off-the-shelf components; moreover, it is designed to be cost-effective and installed in both research laboratories and clinical settings with

---

© 2014 Elsevier Inc. All rights reserved.

Corresponding Authors: Boyd M. Goodson, Department of Chemistry & Biochemistry, Southern Illinois University, Carbondale, IL. Phone: 618-453-6427; Fax: 618-453-6408; bgoodson@chem.siu.edu And Panayiotis (Peter) Nikolaou, Department of Radiology, Vanderbilt University Institute of Imaging Science, Nashville, TN. Phone: 618-203-6912, peter.nikolaou@vanderbilt.edu.

<sup>†</sup>Present address: Cincinnati Children’s Hospital Medical Center, Cincinnati, OH

\*Present address: MD Anderson Cancer Center, Houston, TX

**Publisher's Disclaimer:** This is a PDF file of an unedited manuscript that has been accepted for publication. As a service to our customers we are providing this early version of the manuscript. The manuscript will undergo copyediting, typesetting, and review of the resulting proof before it is published in its final citable form. Please note that during the production process errors may be discovered which could affect the content, and all legal disclaimers that apply to the journal pertain.

materials costing less than \$125,000. The device runs in the xenon-rich regime (up to 1800 Torr Xe in 0.5 L) in either stopped-flow or single-batch mode—making cryo-collection of the hyperpolarized gas unnecessary for many applications. In-cell  $^{129}\text{Xe}$  nuclear spin polarization values of ~30-90% have been measured for Xe loadings of ~300-1600 Torr. Typical  $^{129}\text{Xe}$  polarization build-up and  $T_1$  relaxation time constants were ~8.5 min and ~1.9 hr respectively under our SEOP conditions; such ratios, combined with near-unity Rb electron spin polarizations enabled by the high resonant laser power (up to ~200 W), permits such high  $P_{\text{Xe}}$  values to be achieved despite the high in-cell Xe densities. Importantly, most of the polarization is maintained during efficient HP gas transfer to other containers, and ultra-long  $^{129}\text{Xe}$  relaxation times (up to nearly 6 hr) were observed in Tedlar bags following transport to a clinical 3 T scanner for MR spectroscopy and imaging as a prelude to *in vivo* experiments. The device has received FDA IND approval for a clinical study of COPD subjects. The primary focus of this paper is on the technical / engineering development of the polarizer, with the explicit goals of facilitating the adaptation of design features and operative modes into other laboratories, and of spurring the further advancement of HP-gas MR applications in biomedicine.

## Keywords

hyperpolarization; MRI; laser-polarized xenon; optical pumping; lung imaging

## 1. Introduction

The high sensitivity and biological compatibility of hyperpolarized xenon-129 (HP  $^{129}\text{Xe}$ ) makes it attractive for a wide variety of potential biomedical applications (1-3)—particularly those involving pulmonary medicine (4-15). Xenon's solubility (16) may be exploited to allow studies in bodily tissues (17) including blood (18,19), as well as those involving various biologically compatible liquids (20-22), and its wide chemical shift range and sensitive spin-relaxation response makes HP  $^{129}\text{Xe}$  a useful probe of the local molecular environment (1,23-25), even allowing local blood oxygenation maps as well as spectroscopic studies of flow (9,26-29). While much of the earlier efforts developing HP gases for MR applications concentrated on  $^3\text{He}$ , the world-wide shortage of this isotope (30) (a product of tritium decay) increases the urgency for the development of improved HP  $^{129}\text{Xe}$  approaches, with notable progress over the years (e.g., Refs. (31-39)). Despite these efforts, a major impediment towards wider-scale utilization of HP  $^{129}\text{Xe}$  in clinical applications has been the difficulty of reliably and inexpensively producing large quantities of hyperpolarized xenon with high  $^{129}\text{Xe}$  polarization ( $P_{\text{Xe}}$ ).

In order to facilitate the implementation of HP  $^{129}\text{Xe}$  in biomedical and clinical applications, our collaboration has developed a  $^{129}\text{Xe}$  'hyperpolarizer' for clinical, pre-clinical, and materials research (40). The device prepares HP  $^{129}\text{Xe}$  via the well-established technique of spin-exchange optical pumping (SEOP (41)), where unpaired *electronic* spins of an alkali metal vapor (typically Rb or Cs (42)) are polarized via depopulation optical pumping with circularly polarized laser light, and the polarization is subsequently transferred to xenon *nuclear* spins during gas-phase collisions via the hyperfine interaction. However, unlike most  $^{129}\text{Xe}$  polarization devices (including those from commercial sources), the presently

described hyperpolarizer runs in batch / stopped-flow mode in the high-Xe-density regime (up to 1800 Torr in a 0.5 L cell). In many circumstances this mode of operation obviates, in part, the usual requirement to cryo-collect the HP  $^{129}\text{Xe}$  (e.g., Ref. (43))—a process that otherwise increases design complexity and can also lead to undesirable polarization losses during accumulation, storage, phase transitions, and transfer of HP  $^{129}\text{Xe}$  (44). Cryo-collection also helps ensure that residual Rb from the cell is not transferred to sample containers; thus our device includes a Teflon filter in the transfer line to getter any Rb or other particulate matter that might otherwise enter the sample space. Furthermore, the device is automated, modular, portable, and relatively easy to use, employing an “open-source” design comprised of mostly off-the-shelf components; as described below, many of the initially ‘custom’ components can now be readily purchased from commercial suppliers. Originating from our previous efforts studying batch-mode and stopped-flow (32) SEOP at high Xe densities and resonant laser fluxes (39,45,46), this new scaled-up design can achieve ~1 L/hr production rates, with  $^{129}\text{Xe}$  nuclear spin polarization values ( $P_{\text{Xe}}$ ) of ~90%, ~57%, ~50%, and ~30% for Xe loadings of ~300, ~500, ~760, and ~1570 Torr, respectively (40). Furthermore, little polarization loss is suffered during cell cool-down and gas transfer from the device to sample containers. Long decay times for the HP  $^{129}\text{Xe}$  contrast agent (up to nearly 6 hr) were observed in Tedlar bags following transport to a clinical 3 T scanner. Importantly, XeNA is presently being used for a study involving COPD subjects at Brigham & Women’s Hospital (FDA IND #116,662).

The focus of this paper is on the technical / engineering development and capabilities of the polarizer (47,48). To briefly outline the subsequent sections: The Materials and Methods section focuses on describing the major components of the polarizer in great detail, comprising: (a) the framework design and chassis used to house and setup all the components, (b) the electromagnetic coils, (c) the laser, supporting optics, and optical path, (d) the optical pumping (OP) cell design and preparation including the filling procedure, (e) OP oven design and temperature control components, (f) gas manifold design, major components and vacuum system, (g) description of the (optional) cryo-collection setup and design, (h) microcontroller design, automation control and interface; and (i) *in situ* detection instrumentation. Commercial suppliers and part numbers for components are provided throughout in order to facilitate the construction of this ‘open-source’ device in other labs. The Results section describes the methods used for quality assurance (QA) of the  $P_{\text{Xe}}$  along with examples of  $^{129}\text{Xe}$  MRI from a human subject; for more in-depth analyses and theoretical considerations of the  $P_{\text{Xe}}$  results, please refer to Ref. (40). The Discussion section provides the practical advantages and limitations of the hyperpolarizer, as well as some possible design improvements to be investigated in the future. We briefly note here other  $^{129}\text{Xe}$  polarizers in the literature (e.g., Refs. (31-39,43,49-51)—as well as those from commercial sources (52-54)); those considering assembly or purchase of a polarizer are encouraged to review the designs and capabilities of many devices in light of their own applications, needs, and resources.

## 2. Materials and Methods

Our consortium’s “open-source” automated  $^{129}\text{Xe}$  polarizer (dubbed “XeNA” for XENon polarization Automated), is principally comprised of a mobile chassis, an electromagnetic

coil assembly, a laser system, a vacuum / gas-handling manifold, on-board spectrometers (and other sensors) for QA and feedback, and a computer/automation system (Fig. 1A). The details of the design, components, assembly, and operation of XeNA are provided here and in the corresponding sections of the Supplemental Information documentation.

## 2a. Frame

The lower portion of the framework of this polarizer design consists of two 19 in. rack-mountable cabinets used to house the required hardware (Figs. 1b & Fig. S1). The mobile device is supported by six 4 in. heavy-duty casters (McMaster-Carr, P/N #27075T72). The upper section of the polarizer is constructed from extruded aluminum slotted strut (45 mm × 45 mm) from Minitec Framing, which results in a strong and configurable framework—see Fig. S2 for additional details. The base support of the upper frame is bolted directly to the lower console to support the magnet coils and laser enclosure. The entire optics train and magnet assembly is contained in a light-tight enclosure with a top-mounted door built with Minitec slots rails with attached Alupalite panels (corrugated plastic core with 0.013 in. thick matte black painted aluminum skins on both sides).

## 2b. Magnets

A homogenous magnetic field is provided by a four-coil electromagnet assembly (P/N A650011, Acutran, Fombell, PA—23.6" ID; 12 turns per layer, 17 layers, 12AWG) operating at either 5.26 mT (62.0 kHz  $^{129}\text{Xe}$  frequency) or 1.46 mT (62.0 kHz  $^1\text{H}$  frequency). The magnets are supported by the upper Minitec frame and held in place by 90° angle brackets (Minitec Framing). The four-coil geometry of the electromagnet is that of a Helmholtz pair series inspired by the designs Barker (55) and was optimized using BiotSavart software (Ripplon Software Inc, New Westminster, BC, Canada); a true Barker setup would require varying the number of turns, the current and/or the diameters of the inner versus outer coil pairs. The four-coil electromagnets are connected in series and are powered by a single power supply (Kenwood, P/N PDS60/12).

## 2c. Laser and Optical Path

A single 5.5 foot long optical breadboard (Thor Labs) is bolted to the center of the upper frame to mount the optics and serve as a platform for the laser and optical pumping oven. A custom translational platform (Minitec) with aluminum T-slotted rails is used to hold the laser in position (Fig. 2a). Each T-slotted rail's position can be adjusted without disassembling the frame; this feature allows for simpler adjustment of the optical breadboard position so that the laser optical path and optical pumping cell may be better aligned with the axial isocenter of the four-coil electromagnet set-up. To further aid with the alignment procedures the laser is equipped with a <5 mW visible aiming beam (Fig. S3 *Inset*).

The optical path (Fig. 2b) begins with a 200 W laser diode array (LDA, QPC Lasers, P/N 6507-0001 Brightlock Ultra-500) that produces near-IR laser output that is frequency-narrowed (nominal FWHM~0.27 nm) by 'on-chip' volume holographic gratings (VHGs) (46). The nominal output is resonant with the Rb D<sub>1</sub> line at ~794.8 nm, and is tunable over >1 nm range by adjusting the LDA's temperature, which is maintained by a 800 W water-chiller (K-O Concepts model LCR-8), and the laser driving current (Fig. S1b). This

tunability allows the laser output to be placed on resonance with the Rb absorption center at different output powers (see Fig. S4b), as well as operate detuned for off-resonant SEOP (45,46,56). The laser beam is incident on a short (~6 in.) optical fiber that preserves most (>90%) of the linear polarization and then is expanded and collimated to 2 in. diameter by two lenses. Prior to entering a 2 in. polarizing beam-splitter (PBS) cube, the *s*-polarized beam component (<10% of incident power) is reflected 90° to the right and discarded into a beam block; the main (*p*-polarized) beam is transmitted forward into a quarter-wave ( $\lambda/4$ ) plate, which renders the beam circularly-polarized.

The laser beam enters and exits the optical pumping oven through anti-reflection (AR)-coated optical flats (see below). Upon exiting the rear of the oven the beam is retro-reflected back through the cell via a 3 in. mirror (Thor Labs) and directed into the optics assembly, where the PBS reflects the beam into a second beam block. To provide additional flexibility for the polarizer, all optics were chosen to be sufficiently broad-band to also allow operation with Cs SEOP at 894.3 nm (e.g., Ref. (42)). Except for the PBS and  $\lambda/4$  plate, all components of the optical path assembly attached to the laser were purchased through Thor Labs (See Table S1 and Fig. S3). Due to the high output power of the LDA, cooling fans are installed next to the beam blocks to direct air over their fins (Fig. S3).

## 2d. Optical Pumping Cell

The cell is a custom Pyrex (borosilicate glass) 2 in. diameter cylinder, with flat optical windows at the front and the rear (Mid-Rivers Glassblowing, Inc., St. Charles, MO, P/N MRG934-01A). Each OP-cell is 9.75 in. long with an internal volume of approximately 500 cc. The oven can accommodate variable cell lengths (6 in. – 12 in.). The OP-cells have one opening, sealed by a Chemglass Teflon stopcock that is pneumatically actuated using a Humphrey Rotary Actuator (P/N HRAPS5-360-S) and custom-designed Helical (P/N 9947-26mm-6mm, Item# 28571, Fig. 3d) closing off a ¼ in. O.D. vertical stem trapping the gas content inside the cell.

Prior to installation in the polarizer, each OP-cell is pressure-tested and then prepared as follows. First, each one is soaked in a KOH/methanol base bath for 24 hours to remove impurities from the glass surface. The OP-Cell is then rinsed first with distilled water, and then with methanol. The cell is then placed in a bath ultrasonic cleaner filled with a mixture of methanol and distilled water and sonicated for about 1 hour at room temperature. The cell is then removed and rinsed again with distilled water followed by methanol, and then placed in an oven (110 °C) to dry. The dried OP-cell is coated with a siliconizing agent (SurfaSil, P/N PI-42800, Fisher Scientific) to slow  $^{129}\text{Xe}$   $T_1$  relaxation due to interactions of  $^{129}\text{Xe}$  with paramagnetic centers in the glass (57-59); here, a 10 mL solution is prepared by diluting 1 mL of SurfaSil with hexane. Some of the solution is then pipetted into the cell and shaken to spread the solution over the entire inner surface. The cell is then emptied and washed with ~10 mL of pure hexane. This process is repeated 3 times, ending with a final hexane rinse. The cell is then placed in a warm oven (~60 °C) for at least 1 hour; afterwards, the cell is allowed to cool and its contents evacuated down to  $<1 \times 10^{-3}$  Torr prior to loading the cell in the transfer chamber of a glove box. The cell is then loaded with ~250 mg of molten Rb metal via pipette in the glove box's inert atmosphere. The OP-cell is then

removed from the glove box and evacuated, and the Rb droplet is heated to its melting point to degas it prior to distribution as a thin film on the cell's inner surface via local heating/cooling. Once Rb is distributed, the OP-cell can be placed in the OP-oven to be filled with a gas mixture of ultra-high purity  $^{129}\text{Xe}$  and  $\text{N}_2$ . The  $\text{N}_2$  gas helps suppress unwanted re-emission of unpolarized light from the electronically excited Rb (31) (known as radiation trapping) as well as other undesirable energetic processes (60). Additionally, the  $\text{N}_2$  provides additional collision-broadening of the Rb absorption line, improving the absorption efficiency of the laser (61).

The OP-cell is attached to the polarizer's gas manifold (Fig. 1A) via a ¼ in. PFA Swagelok union T fitting, and is loaded with a gas mixture of  $^{129}\text{Xe}$  and  $\text{N}_2$  automatically. This automation procedure involves evacuating the manifold lines prior to opening the OP-cell to the manifold to prevent oxidation of the Rb metal. The Edwards RV-5 rotary vane mechanical pump is used for achieving initial rough vacuum level ( $>10^{-2}$  Torr) before switching to an Edwards Turbo Pump Station (TS75W). Once a pressure of  $\sim 10^{-4}$ - $10^{-5}$  Torr is achieved, the OP-Cell may be closed. The automation sequence continues by performing three purge/vacuum cycles using ultra-high purity  $\text{N}_2$  gas in preparation to load the OP-cell. Once complete, the desired  $^{129}\text{Xe}/\text{N}_2$  mixture is loaded into the evacuated OP-cell, see Supporting Information for details. Once the OP-cell has been filled, then the optical pumping process can take place.

## 2e. Optical Pumping Oven

The oven is manufactured from non-magnetic materials: Teflon, nylon, and glass that can handle moderately high ( $>120$  °C) operational temperatures (Figs. 3A & S4). The front and the rear walls of the oven contain 3 in. borosilicate (BK7) optical windows with anti-reflection coatings (CVI Melles-Griot P/N W2-PW1-3025-C-670-1064-0) appropriate for the near-IR wavelengths (640-1064 nm). The OP-cell and its contents are heated using a forced-air oven. The oven contains two inlets for heating or cooling air, and one exhaust port (Fig. S4). Since it is necessary to have the polarizer work in areas where compressed-air hook-ups may not be available, the gas supply of the temperature-control system is provided by a self-pressurizing liquid nitrogen dewar. A full dewar can supply sufficient gas for 12+ hours of continuous operation. The oven gas supply is routed through two 400 W heat pipes (Omega Engineering, Stamford, CT, P/N APH-5051) mounted inside an aluminum enclosure (Fig. 3C) and connected to the oven inlets via temperature-resistant silicone tubing (3/4 in. O.D. Silcon®, P/N 2802471, NewAge Industries). The heaters are controlled through a temperature controller (Omega Engineering, Stamford, CT, i-series CNi3244-C24) via feedback from thermocouple sensors inside the OP-Oven.

An opening in the side wall of the oven allows access to the cell's stopcock, which is connected to the Helical-Rotary Actuator. The oven side walls include Pyrex window panels to allow monitoring of the SEOP process with optical probe beams and optimizing the laser beam alignment. The oven is mounted on lateral translational stages to permit fine adjustments to both the front and back of the oven with respect to the laser beam.

## 2f. Gas Manifold

This gas handling system consists of two distinct sections (Figs. 1a & S1a): the ‘upstream’ section contains unpolarized gas used to fill the OP-Cell, and the ‘downstream’ section is used to transfer hyperpolarized  $^{129}\text{Xe}$  to either a Tedlar bag or storage condensation coils. The ‘upstream’ system utilizes solenoid valves (green in Fig. 1a, McMaster-Carr P/N 5077T123 and Parker P/N 099-0167-900) and pneumatically actuated Teflon valves (red in Fig. 1a, Teqcom P/N M222CPFS-T). All valves are automated through the microcontroller box as follows. The valves allow gas flow regulation throughout the entire manifold. The loading ‘upstream’ section of the manifold is built using ¼ in. Swagelok pieces connecting stainless steel tubing and solenoid valves. The Edwards RV5 mechanical roughing pump and Turbo Pump Station are connected to a single vacuum line through a Swagelok T-connector that leads to both ‘upstream’ and ‘downstream’ sections of the gas handling system. It is extremely important to remove all  $\text{O}_2$  from the system as it not only reacts with the alkali metal in the OP-cell, but if present in the transfer lines will quickly de-polarize the hyperpolarized  $^{129}\text{Xe}$  gas.

The gas-handling system is equipped with three cylinders of ultra-high purity natural abundance  $^{129}\text{Xe}$ , enriched  $^{129}\text{Xe}$ , and  $\text{N}_2$  gas (all fitted with CG-580 two-stage regulators), thus allowing the option to use natural abundance or enriched  $^{129}\text{Xe}$ . After passing through oxygen filters/getters (Oxiclear / Labclear, P/N DGP-250-R1), these gases are delivered to the cell via a pulse-damping snubber (McMaster-Carr) that is used to restrict the flow rate of gases. The gas pressures are monitored by two different pressure gauges (for monitoring vacuum and high pressure respectively), which provide feedback to the microcontroller. The ‘fine’ gauge is a Teledyne Hastings HPM 2002, which is responsible for monitoring from ~800 Torr down to the  $10^{-5}$  Torr vacuum range. The ‘coarse’ high-pressure gauge (rated to ~6000 Torr; Omega P/N PX309-100G5V) monitors pressure from 760 to 2000 Torr (total operational in OP-cell pressure).

The ‘downstream’ transfer section of the gas handling system is less complex than the ‘upstream’ loading section and contains fewer valves. Because HP  $^{129}\text{Xe}$  gas can easily be depolarized, all surfaces that may come into contact with the HP  $^{129}\text{Xe}$  must be non-magnetic. As a result, only Teflon components and SurfaSil-coated glass surfaces are used in the ‘downstream’ component of the gas-handling system. Furthermore, the HP  $^{129}\text{Xe}$  contrast agent ejection line is situated within the ambient field of the SEOP electromagnet to prevent any zero-field crossings, which could otherwise depolarize HP  $^{129}\text{Xe}$ . The transfer line is equipped with a gas filter (Entegris Wafergard GT-Plus; WGFG 21K P3; various suppliers, e.g. Venture Technologies Group, Farmington Hills, MI) to getter any residual Rb metal and other micro- and nanoparticles. The HP  $^{129}\text{Xe}$  cryo-collection stage (see below) is optional in the programmed GUI interface, and the condensation coil setup (Fig. 3b) may be installed in the transfer line. As mentioned above, the ‘downstream’ transfer section is also connected to the vacuum system, which evacuates the lines and the Tedlar bag while  $^{129}\text{Xe}$  is being optically polarized in the cell.

## 2g. Cryo-Collection Setup

This setup consists of a custom-made Pyrex tubular spiral storage vessel (Mid-Rivers Glassblowing, Inc., P/N MRG927-01C) that allows the HP  $^{129}\text{Xe}$  to be collected and stored prior to transfer to the Tedlar bag and administration to the subject or sample. The storage coil has Chemglass Teflon stopcock valves on each side of the coil. The spiral coil serves the functions of collecting, storing, and transferring the HP  $^{129}\text{Xe}$ , and its valves are each controlled via a helical-rotary actuator assembly. The coil resides in a strong (>500 Gauss) magnetic field produced by a pair of large permanent magnets (see above and Fig. 3b). The strong field prevents HP  $^{129}\text{Xe}$  depolarization in the solid state through coupling with neighboring (quadrupolar)  $^{131}\text{Xe}$  spins in the solid lattice (62). The magnets are held in place with custom-made aluminum holders with a mounting bar that can be attached directly to the main upper frame (Minitec Framing). The condenser may be cooled with liquid  $\text{N}_2$  (well below the freezing temperature of xenon, allowing  $\text{N}_2$  gas to pass through), and then, prior to the transfer to the Tedlar bag, warmed either with lukewarm water or with heated nitrogen gas. It is important that HP  $^{129}\text{Xe}$  is sublimated rapidly to suppress  $^{129}\text{Xe}$  relaxation that peaks as the xenon motion in the lattice increases, just below the triple point (44).

## 2h. Microcontroller Automation and Interface

The polarizer automation control box (Fig. 4) consists of numerous relays for turning alternating-current (AC) or direct-current (DC) powered devices on or off in a time-dependent sequence with sensor measurements allowing process control. An open-source microcontroller (Arduino Mega 2560 rev3, P/N 1050-1018-ND, Digikey, Thief River Falls, MN) orchestrates all operations. A dual-output power supply (CUI VF-D320-D1224A, P/N 102-2001-ND, Digikey) provides power for the automation control box, a gas valve manifold (Bürkert, Germany, P/N MP11) enabling pneumatic valve operation through 3/2-way solenoids valves (Bürkert, Germany, 6524 Type) of the manifold, and other devices used either in the internal pneumatic manifold or the external gas manifold. The microcontroller digital I/O lines provide activation of the AC or DC solid state relays (SSRs) (Grayhill I/O Relay Module, P/N GH3040-ND or GH-3038-ND, Digikey), thereby selectively powering other devices such as electronic solenoid valves, heaters, instrumentation, etc. Various controller outputs also include activating external devices via TTL level logic, such as shutting down the laser power supply unit (PSU) or triggering the low-field NMR spectrometer (Kea2, Magritek) to run a pulse program. Microcontroller inputs include status changes on digital input lines, and various sensors that can be interacted with via serial communications (see below). Additionally, the micro-controller interacts with a computer graphical user interface (GUI) through commands sent over the built-in USB-serial interface (Fig. S5). All programmed gas manifold load/transfer sequences are stored on the micro-controller board's memory. The GUI itself was designed and programmed in open-source software ([processing.org](http://processing.org)).

Sensor inputs also initiate microcontroller responses. The automation control box features two safety interlocks. The first ensures that the water chiller is on before permitting device operation, whereas the second ensures that the upper frame door is closed during laser operation. The water chiller status is sensed by the water 'low flow' switch (P/N 2371K41,

McMaster-Carr, Aurora, OH). The mechanical safety limit switch sensing the status of the upper frame is P/N 6352K41, McMaster-Carr. Activation of any of these sensors (5V → 0V) results in the following: (i) the laser PSU being sent to standby (laser off), (ii) the OP-cell being closed off to prevent contamination, and (iii) the microcontroller shutting down in a way that requires a physical reset. The pressure sensors described above are monitored by the microcontroller. Oven temperature monitoring and control are achieved by communication between the microcontroller and the oven's temperature controller.

In general operation, the microcontroller runs a loop that obtains temperature and pressure measurements and transmits them to the computer GUI. Interrupt service routines (ISRs) monitor the water flow and door safety switches. Upon receipt of a command from the computer GUI during this general loop, the appropriate function is called after decoding. Such functions can include: oven temperature or manifold pressure level monitoring; timeouts on loops (as in the case of leaks preventing the gas-handling manifold from reaching specified vacuum levels); obtaining user input from the GUI (such as the requested xenon loading pressure); or reporting controller status information. GUI buttons launch automated procedures such as those necessary for replacing gas cylinders or for production of HP  $^{129}\text{Xe}$ .

## 2i. In-situ polarimetry

*In situ* detection is enabled by a low-field high-resolution NMR spectrometer (Kea2, Magritek) and an Ocean Optics HR2000+ high-resolution near-IR spectrometer. The IR probe detecting transmitted laser photons is fiber-optically connected behind the 3 in. retro-reflection mirror, whereas the RF coil (tuned to 62 kHz and matched to 50 Ohms) is located directly under the cell. The low-field NMR spectrometer is used for *in situ* QA of the SEOP process (detecting nuclear spin-polarization of  $^{129}\text{Xe}$ ). *In-situ* NMR detection utilizes a small circular surface coil (~1.5 in. O.D.) with 342 turns using 34 AWG wire. This surface coil was tuned utilizing an Agilent E5071c ENA Series network analyzer for  $^{129}\text{Xe}$  detection at 5.26 mT and  $^1\text{H}$  at 1.46 mT respectively. The corresponding near-IR spectra provide detailed information regarding the status and output quality of the laser, and how well it is being absorbed by the Rb alkali metal in the cell. Additionally, the transmitted laser spectra can be used to infer the average electron spin polarization (40,45), see Supporting Information.

## 3. Results

Four independent methods have been used to determine nuclear and electron spin polarization (40). These methods include (i) *in-situ* (in OP-cell) field-cycled near-IR spectroscopy (45) to probe Rb electron spin polarization; (ii) *in-situ* (in OP-cell)  $^{129}\text{Xe}$  NMR at 5.26 mT; (iii) *ex-situ* HP  $^{129}\text{Xe}$  gas transferred to a "intermediate field" (47.5 mT) of a 122 mm bore magnet (Magritek); and (iv) *ex-situ* HP  $^{129}\text{Xe}$  gas transferred into a Tedlar bag and subsequent  $^{129}\text{Xe}$  NMR/MRI using a clinical 3 T scanner. Excellent agreement was observed among the different approaches used to quantify  $P_{\text{Xe}}$  (see Fig. 6 below). A detailed analysis of these results has been reported previously (40), and thus only a brief discussion is provided here.

The resulting *in-situ* HP  $^{129}\text{Xe}$  NMR spectra (e.g., Fig. 5a) were compared to the spectra of thermally polarized water at the same NMR frequency, allowing in-cell  $P_{\text{Xe}}$  values to be determined; in this example,  $P_{\text{Xe}}=49.5\%\pm 2.8\%$  was achieved for a cell containing 761 Torr Xe. The thermal  $^1\text{H}$  reference signal (Fig. S9a,b) used to calculate  $P_{\text{Xe}}$  was obtained using an identical OP-cell filled with 5 mM  $\text{CuSO}_4$  doped water (63,64). Furthermore, *in-situ* NMR detection allows measurement of build-up and decay of HP  $^{129}\text{Xe}$  during and after SEOP. Examples of different  $P_{\text{Xe}}$  accumulation and  $^{129}\text{Xe}$   $T_1$  relaxation studies are shown in Figs. 5b,c. The  $^{129}\text{Xe}$  polarization build-up and  $T_1$  decay time constants were  $8.5\pm 0.7$  min and  $1.9\pm 0.6$  hr, respectively.

*Ex-situ* detection at 47.5 mT allows for simultaneous evaluation of  $^{129}\text{Xe}$  polarization quality and agent-transfer efficiency. The polarized gas was transferred via a 2 meter long  $\frac{1}{4}$  in. O.D. PTFE tubing into a 52 mL polypropylene spherical phantom located within the field of the 47.5 mT bore magnet system. HP  $^{129}\text{Xe}$  was detected at 559 kHz, whereas a  $^{13}\text{C}$  reference sample was detected at 508 kHz using a broad-band dual-channel RF probe (63). Comparison of the *ex situ* 47.5 mT results with the *in-situ* 5.26 mT  $^{129}\text{Xe}$  NMR polarimetry taken during the same experiment generally showed little loss of  $^{129}\text{Xe}$  polarization during transfer from the SEOP cell (40). Similar efficiencies were observed using *ex-situ* HP  $^{129}\text{Xe}$  spectroscopy at 3 T (40).

HP  $^{129}\text{Xe}$  gas expanded into 800 mL Tedlar bags was used to quantify the relaxation (i.e. life-time of the produced contrast agent) using a clinical 3 T MRI scanner. For most acquisitions, two different storage fields (0.0015 T and 3 T) were used to cover the dynamic range of FDA-approved magnetic fields for clinical MRI use.  $^{129}\text{Xe}$   $T_1$  time constants were  $38\pm 12$  min and  $5.9\pm 0.4$  hr at 1.5 mT and 3 T respectively (40)—results that project positively for a variety of clinical and pre-clinical applications requiring gas-phase storage or accumulation of HP  $^{129}\text{Xe}$ . When polarizing  $^{129}\text{Xe}$  via batch/stopped-flow SEOP without cryo-collection, it is also important that residual Rb does not end up in sample containers. The combination of an efficient cell cool-down procedure (see Supplemental Information) and the use of the Teflon filter in the transfer line (described above) help to ensure that Rb (or other particulate matter) does not end up in the inhaled gas mixture. Following three separate SEOP runs, Tedlar bags were prepared and sent for elemental analysis (Element One, Wilmington, NC). In all cases, Rb content was found to be less than 5 ng / bag.

$^{129}\text{Xe}$  polarization values achieved with various in-cell Xe densities (i.e., with Xe partial pressures between  $\sim 300$ -1600 Torr), over a range of conditions including different magnetic field strengths, NMR acquisition methodologies, etc., are summarized in Fig. 6 (40). The data include values for in-cell  $P_{\text{Xe}}$  values of  $90.9\pm 5.2\%$ ,  $57.1\pm 3.3\%$ ,  $50.1\pm 2.9\%$ , and  $33.4\pm 1.9\%$  measured for Xe loadings of 300, 495, 765, and 1570 Torr, respectively;  $P_{\text{Xe}}$  values of  $41\pm 1.6\%$  and  $28\pm 1.1\%$  with  $\sim 760$  and  $\sim 1545$  Torr Xe loadings were obtained following transfer to Tedlar bags and subsequent transport to the 3 T scanner.

The polarizer has recently received FDA Investigational New Drug and IRB regulatory approval for use in a clinical study of COPD patients. Towards that end, the polarizer has already been used in several preliminary  $^{129}\text{Xe}$  MR imaging and spectroscopic experiments involving individual healthy human subjects; for example, images obtained in one

experiment are shown in Fig. 7. For this experiment, a gas mixture comprised of 1300 Torr of 86%-enriched  $^{129}\text{Xe}$  gas and 700 Torr  $\text{N}_2$  gas was loaded and hyperpolarized in the OP-cell. Prior to use,  $P_{\text{Xe}}$  was measured to be 25% in the cell—somewhat lower than typical values (see Fig. 6), owing to the utilization of a OP-cell that was thermally regenerated following partial oxidation during installation. Some of the cell contents were then transferred to a 0.8 L Tedlar bag via expansion (thus, xenon comprised two-thirds of the bag contents). The bag was then transported to a Siemens 3 T clinical MRI scanner and the HP  $^{129}\text{Xe}$  agent was administered to a healthy human volunteer using the following inhalation protocol: the subject completed two full respiration cycles (total lung capacity (TLC) to functional residual capacity, (FRC),  $\times 2$ ), before being asked to inhale contents from the bag (followed by a small gulp of air to help push HP  $^{129}\text{Xe}$  out beyond the trachea). The demonstrated signal strength and image quality achieved are sufficient for the polarizer to support a number of potential pulmonary functional imaging/spectroscopic studies—the subject of future efforts.

#### 4. Discussion

The  $^{129}\text{Xe}$  polarization values summarized here (40) represent by a significant margin the highest yet achieved at such high in-cell Xe densities—and establish the feasibility of attaining near-unity polarization in single (or multiple) batches with HP  $^{129}\text{Xe}$  quantities sufficient for most clinical uses ( $\sim 1$  L/hr). Furthermore, the hyperpolarizer is automated, modular, portable, and easy to maintain. XeNA is built mostly of commercially available components, and the complete material costs for construction were under \$125,000.

The overall performance of the hyperpolarizer stems from a number of technical improvements of stopped-flow high-xenon-pressure SEOP process described here and fundamental improvements reported earlier (40). For instance, the VHG technology combined with high laser power ( $\sim 170$  W) provides high resonant photon flux through the cell. Next, to prevent any dark regions near the edges or longitudinal optical nodes of the OP-cell that could affect the SEOP process, the optical path setup was designed with care as to (i) reduce the loss of laser power through the optical train while expanding to a 2 in. diameter beam and (ii) to illuminate the OP-cell volume with near-unity circular polarization of the incident laser light. Furthermore, we have shown that retro-reflection of the beam back into the cell can provide a  $\sim 30\%$  increase in HP  $^{129}\text{Xe}$  (45). Careful control of the cell temperature is key for SEOP optimization. Previously it was shown that there can be an inverse relationship between Xe density and the optimal temperature for SEOP (e.g., where lower cell temperatures are favored for higher Xe densities (39,46)—particularly when using spectrally-narrowed pump lasers). The steady-state  $^{129}\text{Xe}$  nuclear spin polarization is given by:

$$P_{\text{Xe}}(t=\infty) = \frac{\gamma_{\text{SE}}}{\gamma_{\text{SE}} + \Gamma_{\text{Xe}}} \cdot \langle P_{\text{Rb}} \rangle, \quad (1)$$

where  $\gamma_{\text{SE}}$  is the Rb/Xe spin exchange rate ( $\infty[\text{Rb}]$ ),  $\Lambda_{\text{Xe}}$  is the  $^{129}\text{Xe}$  nuclear spin destruction rate ( $=1/T_1$ ), and  $\langle P_{\text{Rb}} \rangle$  is the volume-averaged Rb electron spin polarization. For example, if one assumes that the intrinsic cell  $^{129}\text{Xe}$   $T_1$  values are similar from cell to

cell (and only mildly sensitive to the small differences in Xe loading or total pressure (65)), the time constants from the curves in Fig. 5 would correspond to ~12-fold larger  $\gamma_{SE}$  value compared to  $\Lambda_{Xe}$ , contributing to the efficiency of the  $^{129}\text{Xe}$  polarization process. Thus overall, the high in-cell  $^{129}\text{Xe}$  polarization values reported here are achieved primarily by: (i) maintaining a high “photon-to-Rb” ratio throughout the cell, thereby ‘forcing’ near-unity  $P_{Rb}$  despite the high Rb electron spin-destruction rates encountered at high Xe densities (66); and (ii) obtaining very slow  $^{129}\text{Xe}$  intrinsic relaxation rates, ensuring high  $\gamma_{SE}:\Lambda_{Xe}$  ratios despite the relatively modest Rb number densities expected at our mild operational oven temperatures (67).

High  $^{129}\text{Xe}$  polarization/collection efficiency is also promoted by the following: (i) the high quality and uniformity of the Rb coating within the cell; (ii) the presence of *in situ* real-time monitoring and feedback of the SEOP process of the Rb spectral absorption and  $^{129}\text{Xe}$  NMR signal; (iii) optimization of OP-cell cool-down procedure prior to transfer of the hyperpolarized contrast agent (discussed in detail in section ‘i’ of the Supporting Information); (iv) suppressing exposure to  $\text{O}_2$  and other paramagnetic materials throughout the gas lines; (v) rapid transfer of HP  $^{129}\text{Xe}$  contrast agent into a Tedlar transportation/delivery bag; and (vi) avoiding Xe phase transitions and other relaxation-susceptible portions of the Xe phase diagram (44).

Although Xe cryo-collection and subsequent sublimation prior to transfer to the sample is optional for XeNA, operation without cryo-collection does result in dilution of the HP  $^{129}\text{Xe}$  with  $\text{N}_2$  gas and leaves behind a significant fraction of the SEOP mixture in the OP-cell following the transfer process after contrast agent preparation. However, both of these issues can be mitigated by (i) using Xe-rich mixtures demonstrated here; (ii) the addition of a large automated gas piston or balloon (32,51), where the cell contents can be expanded into a much larger volume prior to transfer to the sample or transport vessel; and (iii) selecting the ‘topping-off’ procedure implemented in XeNA, which also slightly increases the device duty cycle. Indeed, when preparing multiple bags of HP  $^{129}\text{Xe}$ , this has become the standard mode of operation. Under these typical conditions, the time to produce each bag is ~35-40 min; ~15-20 min is spent polarizing the  $^{129}\text{Xe}$ , with the remaining time being used to purge/evacuate gas lines, transfer gases to and from the cell, and heat up / cool down the OP-cell before and after SEOP.

Future improvements may include (i) the re-designing of the OP-oven, because the current design makes installation and removal of the OP-cell somewhat difficult; (ii) the pressurized liquid  $\text{N}_2$  dewar can be replaced by a more suitable solution for gas heating and cooling to make the polarizer a true stand-alone device; (iii) The LDA and the optical train could be integrated into a single device for easier alignment with the OP-cell (see Supplemental Information); (iv) improving the thermal management of the cell to better mitigate any deleterious effects of high internal gas temperatures (68,69); (v) increased level of automation and components’ integration; (vi) utilization of pre-mixed Xe/ $\text{N}_2$  gas sources, allowing the duty cycle to be increased; and (vii) increasing the simplicity of the polarization procedures would be key for making a true “push-button” operated device. The current device increases the prospects of more widespread implementation of HP  $^{129}\text{Xe}$  MR technology, thus allowing feedback for future improvements.

## 5. Conclusion

We have described here a clinical-scale (~1 L/hr) hyperpolarizer that produces batches of spin-polarized  $^{129}\text{Xe}$  sufficient for clinical examination, with emphasis on specific design features and practical aspects of operation. The polarizer's 'open-source' design and automation should facilitate implementation of HP  $^{129}\text{Xe}$  technology into clinical and pre-clinical settings. Four independent methods for characterizing the spin polarization have been utilized, and up to 90%  $^{129}\text{Xe}$  polarization is achieved. Efficient transfer of HP  $^{129}\text{Xe}$  from OP-cells into other sample containers was demonstrated, including Tedlar bags filled with up to 800 mL of polarized gas mixture for clinical imaging. The  $T_1$  of HP  $^{129}\text{Xe}$  was nearly 6 hr in a Tedlar bag used for the contrast agent delivery/transportation from the polarizer to a human volunteer. The ability to achieve high  $P_{\text{Xe}}$  values at high Xe densities, combined with stopped-flow operation and efficient Rb condensation / gettingting, negates the usual requirement of Xe cryo-accumulation and storage, and also should provide improved polarization efficiency for quadrupolar isotopes (e.g.  $^{83}\text{Kr}$  and  $^{131}\text{Xe}$  (3,70-72)).

## Supplementary Material

Refer to Web version on PubMed Central for supplementary material.

## Acknowledgments

We thank B. Saam and G. Schrank for helpful conversations, and E. Koehnemann (Midrivers Glassblowing, Inc.) for expert glassblowing. We also thank John Gore for his support for polarizer construction, and S. Barcus for assistance during the early stages of polarizer construction. N.W. was supported by an NSF post-doctoral fellowship (OISE-0966393); B.M.G. and B.M.G. were supported in part by the NSF (DMR 0852004 & 1157058). This work was funded by NIH (1R01 HL096471) and SIU OSPA. M.J.B. is supported by the School of Medicine, U. Nottingham, UK. E.Y.C. thanks the support from NIH/NCI 5R00 CA134749-03 and DoD CDMRP Era of Hope Award W81XWH-12-1-0159/BC112431. A.M.C. thanks the support from training NIH grant R25 CA136440.

## Abbreviations

<b>AR</b>	Anti-Reflection
<b>COPD</b>	Chronic Obstructive Pulmonary Disease
<b>FOV</b>	Field Of View
<b>FRC</b>	Functional Residual Capacity
<b>FWHM</b>	Full Width Half Max
<b>GRE</b>	Gradient Echo
<b>GUI</b>	Graphical User Interface
<b>HP <math>^{129}\text{Xe}</math></b>	Hyperpolarized Xenon-129
<b>I.D.</b>	Inner Diameter
<b>IR</b>	Infra Red
<b>ISRs</b>	Input Service Routines
<b>KOH</b>	Potassium Hydroxide

<b>LDA</b>	Laser Diode Array
<b>OP</b>	Optical Pumping
<b>O.D.</b>	Outer Diameter
<b>PBS</b>	Polarizing Beam Splitter
<b>PFA</b>	Perfluoroalkoxy
<b>PSU</b>	Power Supply Unit
<b>P<sub>Rb</sub></b>	Rubidium Polarization
<b>P<sub>Xe</sub></b>	Xenon Polarization
<b>QA</b>	Quality Assurance
<b>SAR</b>	Specific Absorption Rate
<b>SEOP</b>	Spin-Exchange Optical Pumping
<b>SNR</b>	Signal-to-Noise Ratio
<b>SSR</b>	Solid-State Relay
<b>TE</b>	echo time
<b>TLC</b>	Total Lung Capacity
<b>TR</b>	repetition time
<b>VHG</b>	Volume Holographic Grating
<b>XeNA</b>	XENon polarizatioN Automated

## References

1. Goodson BM. Nuclear magnetic resonance of laser-polarized noble gases in molecules, materials, and organisms. *J Magn Reson.* 2002; 155(2):157–216. [PubMed: 12036331]
2. Bifone A, Cherubini A. Hyperpolarised Xenon in Biology. *Prog Nucl Magn Reson Spectrosc.* 2003; 42(1-2):1–30.
3. Lilburn D, Pavlovskaya G, Meersmann T. Perspectives of hyperpolarized noble gas MRI beyond He-3. *J Magn Reson.* 2013; 229:173–186. [PubMed: 23290627]
4. Mugler J, Altes T. Hyperpolarized <sup>129</sup>Xe MRI of the human lung. *J Magn Reson Imaging.* 2013; 37:313–331. [PubMed: 23355432]
5. Albert M, Cates G, Driehuys B, Happer W, Saam B, Springer C, Wishnia A. Biological Magnetic Resonance Imaging Using Laser Polarized Xe-129. *Nature.* 1994; 370:199–201. [PubMed: 8028666]
6. Mugler JP, Driehuys B, Brookeman JR, Cates GD, Berr SS, Bryant RG, Daniel TM, deLange EE, Downs JH, Erickson CJ, Happer W, Hinton DP, Kassel NF, Maier T, Phillips CD, Saam BT, Sauer KL, Wagshul ME. MR imaging and spectroscopy using hyperpolarized Xe-129 gas: Preliminary human results. *Magn Reson Med.* 1997; 37(6):809–815. [PubMed: 9178229]
7. Leawoods JC, Yablonskiy DA, Saam B, Gierada DS, Conradi MS. Hyperpolarized He-3 gas production and MR imaging of the lung. *Concepts Magn Reson.* 2001; 13(5):277–293.
8. Moller HE, Chen XJ, Saam B, Hagspiel KD, Johnson GA, Altes TA, Lange EEd, Kauczor H-U. MRI of the Lungs Using Hyperpolarized Noble Gases. *Magn Reson Med.* 2002; 47:1029–1051. [PubMed: 12111949]

9. Patz S, Hersman FW, Muradian I, Hrovat MI, Ruset IC, Ketel S, Jacobson F, Topulos GP, Hatabu H, Butler JP. Hyperpolarized Xe-129 MRI: A viable functional lung imaging modality? *Eur J Radiol.* 2007; 64(3):335–344. [PubMed: 17890035]
10. Dregely JPM I, III, Ruset IC, Altes TA, Mata JF, Miller W, Ketel J, Ketel S, Distelbrink J, Hersman FW, Ruppert K. Hyperpolarized Xenon-129 Gas-Exchange Imaging of Lung Microstructure: First Case Studies in Subjects With Obstructive Lung Disease. *J Magn Reson Imaging.* 2011; 33:1052–1062. [PubMed: 21509861]
11. Kaushik SS, Cleveland ZI, Cofer GP, Metz G, Beaver D, Nouls J, Kraft M, Auffermann W, Wolber J, McAdams HP, Driehuys B. Diffusion-Weighted Hyperpolarized  $^{129}\text{Xe}$  MRI in Healthy Volunteers and Subjects With Chronic Obstructive Pulmonary Disease. *Magn Reson Med.* 2011; 65:1155–1165.
12. Matsuoka S, Patz S, Albert M, Sun Y, Rizi R, Geftter W, Hatabu H. Hyperpolarized Gas MR Imaging of the Lung: Current Status as a Research Tool. *J Thorac Imaging.* 2009; 24:181–188. [PubMed: 19704321]
13. Wild J, Marshall H, Xu X, Norquay G, Parnell S, Clemence M, Griffiths P, Parra-Robles J. Simultaneous Imaging of Lung Structure and Function with Triple-Nuclear Hybrid MR Imaging. *Radiology.* 2013; 267:251–255. [PubMed: 23264344]
14. Lilburn DML, Hughes-Riley T, Six JS, Stupic KF, Shaw DE, Pavlovskaya GE, Meersmann T. Validating Excised Rodent Lungs for Functional Hyperpolarized Xenon-129 MRI. *PLoS One.* 2013; 8(8):e73468. [PubMed: 24023683]
15. Kadlecsek S, Mongkolwisetwara P, Xin Y, Ishii M, Profka H, Emami K, Rizi R. Regional determination of oxygen uptake in rodent lungs using hyperpolarized gas and an analytical treatment of intrapulmonary gas redistribution. *NMR Biomed.* 2011; 24(10):1253–1263. [PubMed: 21387449]
16. Chen RY, Fan FC, Kim S, Jan KM, Usami S, Chien S. Tissue-blood partition coefficient for xenon: temperature and hematocrit dependence. *J Appl Physiology.* 1980; 49:178–183.
17. Swanson SD, Rosen MS, Coulter KP, Welsh RC, Chupp TE. Distribution and Dynamics of Laser-Polarized  $^{129}\text{Xe}$  Magnetization In Vivo. *Magn Reson Med.* 1999; 42:1137–1145. [PubMed: 10571936]
18. Bifone A, Song YQ, Seydoux R, Taylor RE, Goodson BM, Pietrass T, Budinger TF, Navon G, Pines A. NMR of laser-polarized xenon in human blood. *Proc Natl Acad Sci USA.* 1996; 93(23):12932–12936. [PubMed: 8917521]
19. Albert M, Schepkin V, Budinger T. Measurement of Xe-129  $T_1$  in blood to explore the feasibility of hyperpolarized Xe-129 MRI. *J Comput Assist Tomog.* 1995; 19:975–978.
20. Acosta RH, Blümmler P, Münnemann K, Spiess H-W. Mixture and dissolution of laser polarized noble gases: Spectroscopic and imaging applications. *Prog Nucl Magn Reson Spectrosc.* 2012; 66:40–69. [PubMed: 22980033]
21. Goodson BM. Using injectable carriers of laser-polarized noble gases for enhancing NMR and MRI. *Concepts Magnetic Res.* 1999; 11(4):203–223.
22. Venkatesh A, Zhao L, Balamore D, Jolesz F, Albert M. Evaluation of carrier agents for hyperpolarized xenon MRI. *NMR Biomed.* 2000; 13:245–252. [PubMed: 10867704]
23. Rubin SM, Spence MM, Goodson BM, Wemmer DE, Pines A. Evidence of nonspecific surface interactions between laser-polarized xenon and myoglobin in solution. *Proc Natl Acad Sci USA.* 2000; 97:9472–9475. [PubMed: 10931956]
24. Jansch HJ, Gerhard P, Koch M. Xe-129 on Ir(111): NMR study of xenon on a metal single crystal surface. *Proc Natl Acad Sci USA.* 2004; 101(38):13715–13719. [PubMed: 15361579]
25. Schröder L, Lowery TJ, Hilty C, Wemmer DE, Pines A. Molecular imaging using a targeted magnetic resonance hyperpolarized biosensor. *Science.* 2006; 314(5798):446–449. [PubMed: 17053143]
26. Mazzanti M, Walvick R, Zhou X, Sun Y, Shah N, Mansour J, Gereige J, Albert M. Distribution of Hyperpolarized Xenon in the Brain Following Sensory Stimulation: Preliminary MRI Findings. *PLoS One.* 2011; 6:e21607. [PubMed: 21789173]
27. Wolber J, Cherubini A, Leach M, Bifone A. Hyperpolarized Xe-129 NMR as a probe for blood oxygenation. *Magn Reson Med.* 2000; 43:491–496. [PubMed: 10748422]

28. Dabaghyan M, Dregely I, Muradian I, Hrovat M, Hatabu H, Patz S. Oxygen Partial Pressure and Uptake in the Lung with Hyperpolarized  $^{129}\text{Xe}$  MRI: Preliminary Results. Stockholm, Sweden. Proc. Intl. Soc. Magn. Reson. Med. 2010
29. Leung G, Norquay G, Wild JM.  $^{129}\text{Xe}$  as an in vivo probe for MR oximetry. Proc Intl Soc Mag Reson Med. 2013; 21:0816.
30. Shea, DA.; Morgan, D. The Helium-3 Shortage: Supply, Demand, and Options for Congress. 2010.
31. Driehuys B, Cates GD, Miron E, Sauer K, Walter DK, Happer W. High-volume production of laser-polarized Xe-129. Appl Phys Lett. 1996; 69(12):1668–1670.
32. Rosen MS, Chupp TE, Coulter KP, Welsh RC, Swanson SD. Polarized  $^{129}\text{Xe}$  optical pumping/spin exchange and delivery system for magnetic resonance spectroscopy and imaging studies. Rev Sci Instrum. 1999; 70(2):1546–1552.
33. Ruth U, Hof T, Schmidt J, Fick D, Jansch HJ. Production of nitrogen-free, hyperpolarized  $^{129}\text{Xe}$  gas. Appl Phys B. 1999; 68(1):93–97.
34. Zook AL, Adhyaru BB, Bowers CR. High capacity production of > 65% spin polarized xenon-129 for NMR spectroscopy and imaging. J Magn Reson. 2002; 159(2):175–182. [PubMed: 12482697]
35. Mortuza MG, Anala S, Pavlovskaya GE, Dieken TJ, Meersmann T. Spin-exchange optical pumping of high-density xenon-129. J Chem Phys. 2003; 118(4):1581–1584.
36. Knagge K, Prange J, Raftery D. A continuously recirculating optical pumping apparatus for high xenon polarization and surface NMR studies. Chem Phys Lett. 2004; 397:11–16.
37. Ruset IC, Ketel S, Hersman FW. Optical Pumping System Design for Large Production of Hyperpolarized  $^{129}\text{Xe}$ . Phys Rev Lett. 2006; 96(5):053002. [PubMed: 16486926]
38. Schrank G, Ma Z, Schoeck A, Saam B. Characterization of a low-pressure high-capacity Xe-129 flow-through polarizer. Phys. Rev. A. 2009; 80(6)
39. Whiting N, Nikolaou P, Eschmann NA, Barlow MJ, Goodson BM. Interdependence of Xenon Density and Temperature on Rb/ $^{129}\text{Xe}$  Optical Pumping Efficiency at High Xenon Densities. J Magn Reson. 2011; 208(2):298–304. [PubMed: 21185208]
40. Nikolaou P, Coffey A, Walkup L, Gust B, Whiting N, Newton H, Barcus S, Muradyan I, Moroz GD, Rosen M, Patz S, Barlow MJ, Chekmenev E, Goodson BM. Near-unity nuclear polarization with an open-source  $^{129}\text{Xe}$  hyperpolarizer for NMR and MRI. Proc Natl Acad Sci USA. 2013; 110(35):14150–14155. [PubMed: 23946420]
41. Walker T, Happer W. Spin-exchange optical pumping of noble-gas nuclei. Rev Mod Phys. 1997; 69(2):629–642.
42. Whiting N, Eschmann NA, Barlow MJ, Goodson BM.  $^{129}\text{Xe}/\text{Cs}$  (D1, D2) Versus  $^{129}\text{Xe}/\text{Rb}$  (D1) Spin-Exchange Optical Pumping at High Xenon Densities Using High-Power Laser Diode Arrays. Phys Rev A. 2011; 83(5):053428.
43. Six J, Hughes-Riley T, Stupic K, Pavlovskaya G, Meersmann T. Pathway to Cryogen Free Production of Hyperpolarized Krypton-83 and Xenon-129. PLoS One. 2012; 7:e49927. [PubMed: 23209620]
44. Kuzma NN, Patton B, Raman K, Happer W. Fast nuclear spin relaxation in hyperpolarized solid Xe-129. Phys Rev Lett. 2002; 88:147602. [PubMed: 11955177]
45. Nikolaou P, Whiting N, Eschmann NA, Chaffee KE, Goodson BM, Barlow M. Generation of Laser-Polarized Xenon Using Fiber-Coupled Laser Diode Arrays Narrowed with Integrated Volume Holographic Gratings. J Magn Reson. 2009; 197(2):249–254. [PubMed: 19162517]
46. Whiting N, Nikolaou P, Eschmann NA, Goodson BM, Barlow MJ, Lammert R, Ungar J, Vaissie L. Using frequency-narrowed, tunable laser diode arrays with integrated volume holographic gratings for Rb/ $^{129}\text{Xe}$  spin-exchange optical pumping at high resonant laser fluxes and high xenon densities. Appl Phys B. 2012; 106(4):775–788.
47. Nikolaou P, Coffey A, Walkup L, Gust B, Whiting N, Moroz GD, Rosen M, Chekmenev E, Barlow MJ, Patz S, Goodson BM. Towards the Development of an ‘Open-Source’ High Volume  $^{129}\text{Xe}/\text{SEOP}$  Apparatus for Potential Application in Human Lung Imaging and NMR/MRI Studies of Porous Materials. Frontiers in Biomedical Imaging. 2011; III
48. Nikolaou, P.; Coffey, A.; Walkup, L.; Gust, B.; Whiting, N.; Newton, H.; Barcus, S.; Muradyan, I.; Moroz, GD.; Rosen, M.; Patz, S.; Barlow, MJ.; Chekmenev, E.; Goodson, BM. An ‘Open-

- Source'  $^{129}\text{Xe}$  Polarizer for Clinical Imaging, in vivo MRS/MRI, and NMR/MRI of Porous Materials. Miami, FL: 2012.
49. Korchak S, Kilian W, Mitschang L. Configuration and Performance of a Mobile Xe-129 Polarizer. *Appl Magn Reson*. 2013; 44:65–80. [PubMed: 23349565]
  50. Witte C, Kunth M, Döpfert J, Rossella F, Schröder L. Hyperpolarized Xenon for NMR and MRI Applications. *J Vis Exp*. 2012; 67:e4268.
  51. Hughes-Riley T, Six JS, Lilburn DML, Stupic KF, Dorkes AC, Shaw DE, Pavlovskaya GE, Meersmann T. Cryogenics free production of hyperpolarized  $^{129}\text{Xe}$  and  $^{83}\text{Kr}$  for biomedical MRI applications. *J Magn Reson*. 2013; 237:23–33. [PubMed: 24135800]
  52. XeMed LLC. [www.xemed.com](http://www.xemed.com)
  53. Polarean, Inc. [www.polarean.com](http://www.polarean.com)
  54. Toyoko Kagaku. [http://www.toyokokagaku.co.jp/english/product/02\\_02.html](http://www.toyokokagaku.co.jp/english/product/02_02.html)
  55. Barker JR. New Coil Systems for the Production of Uniform Magnetic Fields. *J Sci Instrum*. 1949; 26(8):273.
  56. Parnell SR, Deppe M, Parra-Robles J, Wild JM. Enhancement of  $^{129}\text{Xe}$  polarization by off-resonant spin exchange optical pumping. *J Appl Phys*. 2010; 108:064908.
  57. Breeze SR, Lang S, Moudrakovski I, Ratcliffe CI, Ripmeester JA, Simard B, Santyr G. Coatings for optical pumping cells and extending the lifetime of hyperpolarized xenon. *J Appl Phys*. 1999; 86(7):4040–4042.
  58. Breeze SR, Lang S, Moudrakovski I, Ratcliffe CI, Ripmeester JA, Santyr G, Simard B, Zuger I. Coatings for Optical Pumping Cells and Short-Term Storage of Hyperpolarized Xenon. *J Appl Phys*. 2000; 87:8013–8017.
  59. Zeng X, Miron E, Van Wijngaarden WA, Schreiber D, Happer W. Wall relaxation of spin polarized  $^{129}\text{Xe}$  nuclei. *Phys Lett A*. 1983; 96(4):191–194.
  60. Saha I, Nikolaou P, Whiting N, Goodson BM. Characterization of violet emission from Rb optical pumping cells used in laser-polarized xenon NMR experiments. *Chem Phys Lett*. 2006; 428(4-6): 268–276.
  61. Romalis MV, Miron E, Cates GD. Pressure broadening of Rb D-1 and D-2 lines by He-3, He-4, N-2, and Xe: Line cores and near wings. *Phys Rev A*. 1997; 56(6):4569–4578.
  62. Cates GD, Benton DR, Gatzke M, Happer W, Hasson KC, Newbury NR. Laser production of large nuclear-spin polarization in frozen xenon. *Phys Rev Lett*. 1990; 65:2591–2594. [PubMed: 10042636]
  63. Coffey AM, Shchepin RV, Wilkens K, Waddell KW, Chekmenev EY. A large volume double channel  $^1\text{H}$ -X RF probe for hyperpolarized magnetic resonance at 0.0475 T. *J Magn Reson*. 2012; 220:94–101. [PubMed: 22706029]
  64. Waddell KW, Coffey AM, Chekmenev EY. In situ Detection of PHIP at 48 mT: Demonstration using a Centrally Controlled Polarizer. *J Am Chem Soc*. 2011; 133(1):97–101. [PubMed: 21141960]
  65. Anger BC, Schrank G, Schoeck A, Butler KA, Solum MS, Pugmire RJ, Saam B. Gas-phase spin relaxation of  $^{129}\text{Xe}$ . *Phys Rev A*. 2008; 78(4):043406.
  66. Bouchiat MA, Brossel J, Pottier LC. Evidence for RbRareGas Molecules from the Relaxation of Polarized Rb Atoms in a Rare Gas. *Experimental Results. J Chem Phys*. 1972; 56:3703–3714.
  67. Steck DA. Rb 85 & 87; Cs D-line Data. 20102008
  68. Walter DK, Griffith WM, Happer W. Energy transport in high-density spin-exchange optical pumping cells. *Phys Rev Lett*. 2001; 86:3264–3267. [PubMed: 11327946]
  69. Newton H, Walkup LL, Whiting N, West L, Carriere J, Havermeyer F, Ho L, Morris P, Goodson BM, Barlow MJ. Comparative study of in situ  $\text{N}_2$  rotational Raman spectroscopy methods for probing energy thermalisation processes during spin-exchange optical pumping. *Appl Phys B*. 2013 DOI 10.1007/s00340-013-5588-x.
  70. Cleveland ZI, Pavlovskaya GE, Stupic KF, LeNoir CF, Meersmann T. Exploring hyperpolarized  $^{83}\text{Kr}$  by remotely detected NMR relaxometry. *J Chem Phys*. 2006; 124(4):044312. [PubMed: 16460167]

71. Stupic KF, Cleveland ZI, Pavlovskaya GE, Meersmann T. Quadrupolar Relaxation of Hyperpolarized Krypton-83 as a Probe for Surfaces. *Solid State Nucl Magn Reson.* 2006; 29:79–84. [PubMed: 16202568]
72. Stupic KF, Cleveland ZI, Pavlovskaya GE, Meersmann T. Hyperpolarized  $^{131}\text{Xe}$  NMR spectroscopy. *J Magn Reson.* 2011; 208:58–69. [PubMed: 21051249]

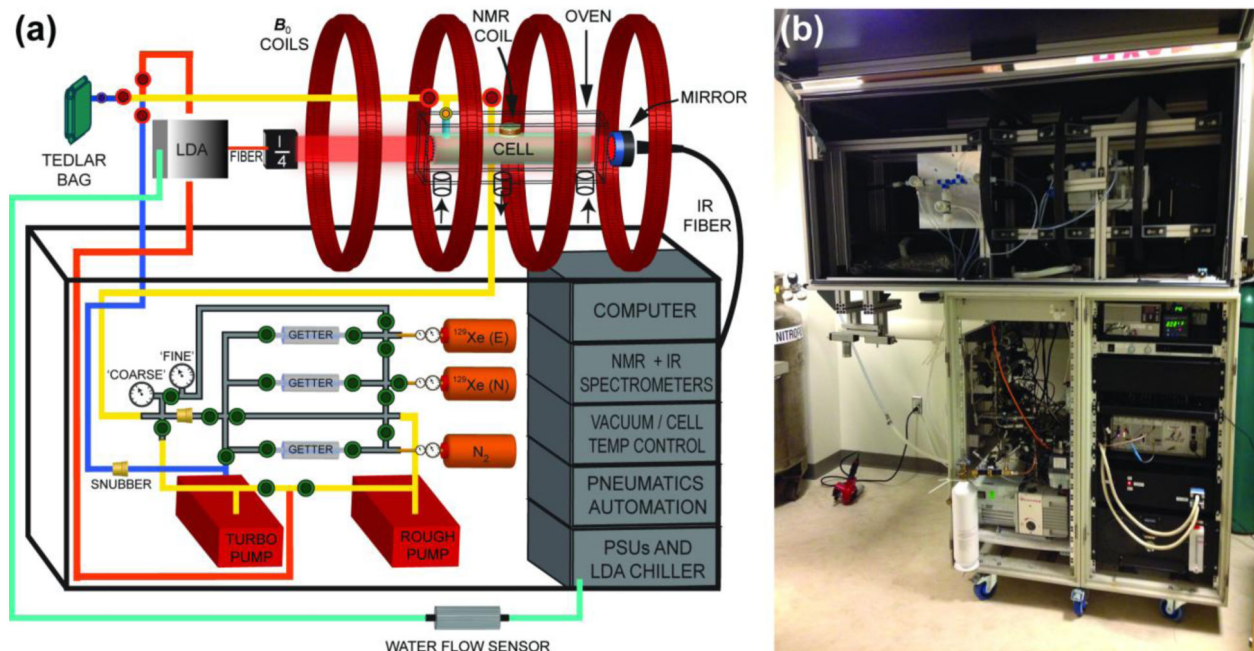


**Figure 1.**

The XeNA polarizer. (a) of the polarizer's key components (the self-pressurized liquid  $N_2$  dewar that provides gas for heating and cooling of the oven and  $N_2$  gas cylinder used to operate pneumatic valves are not shown) (40). The optical path is represented by (" $\lambda/4$ ") and is comprised of beam expanding optics, polarizing beam-splitter cube, quarter-wave plate, and heat sinks (see Fig. 2). For the gas cylinders, "N" and "E" designate xenon with naturally-abundant  $^{129}\text{Xe}$  and isotopically-enriched  $^{129}\text{Xe}$ , respectively (40). (b) Photograph of XeNA with open laser enclosure in its current location in a clinical MRI suite at Brigham and Womens' Hospital, Boston, MA, USA.

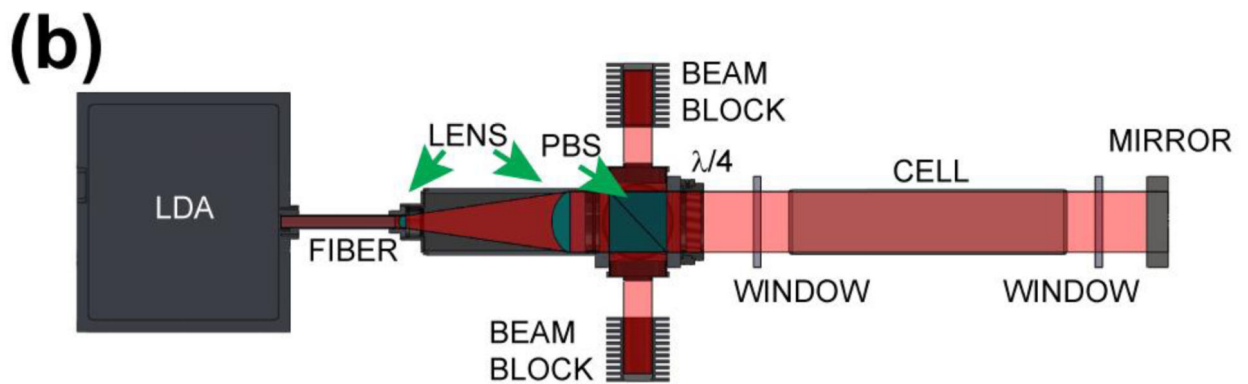
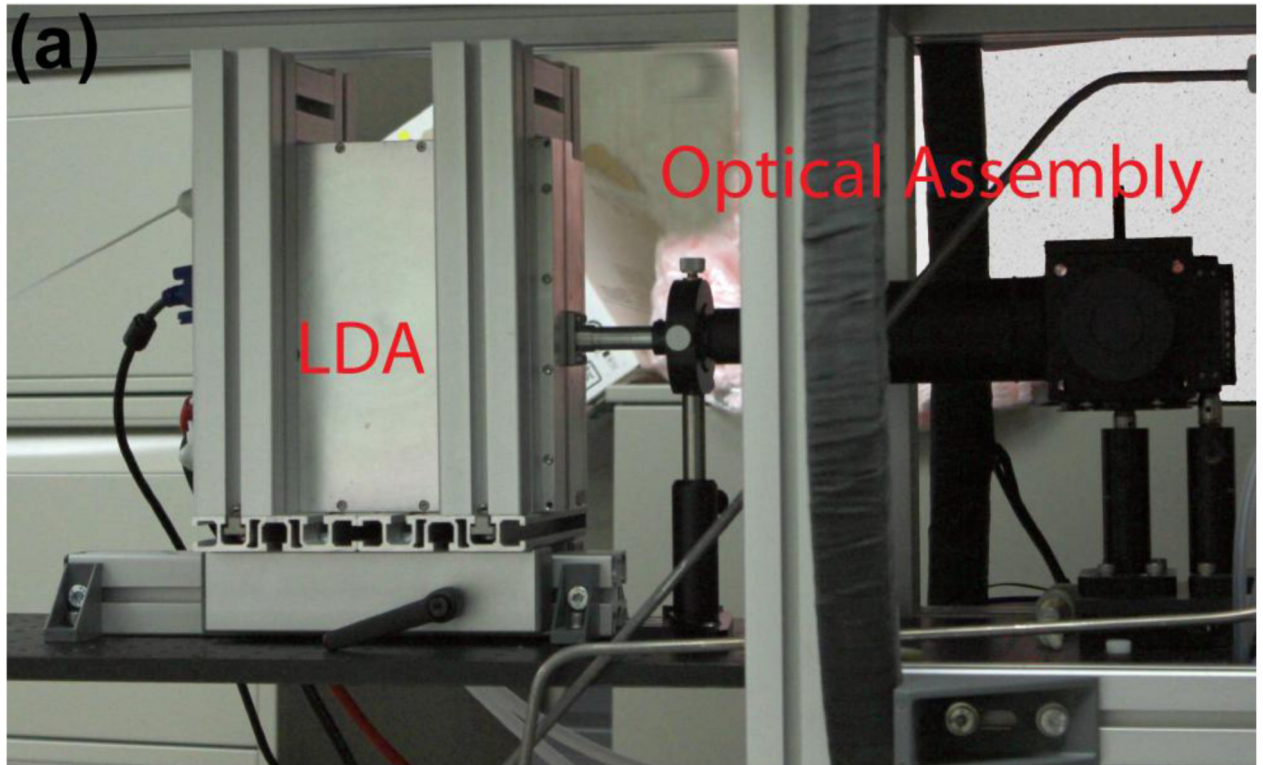


**Figure 2.**

(a) Laser diode array with translational mounting frame, and optical path assembly. (b) Schematic showing the principal elements of the optical path (40). The beam blocks are drawn separated from the polarizing beam splitter (PBS) housing for clarity.

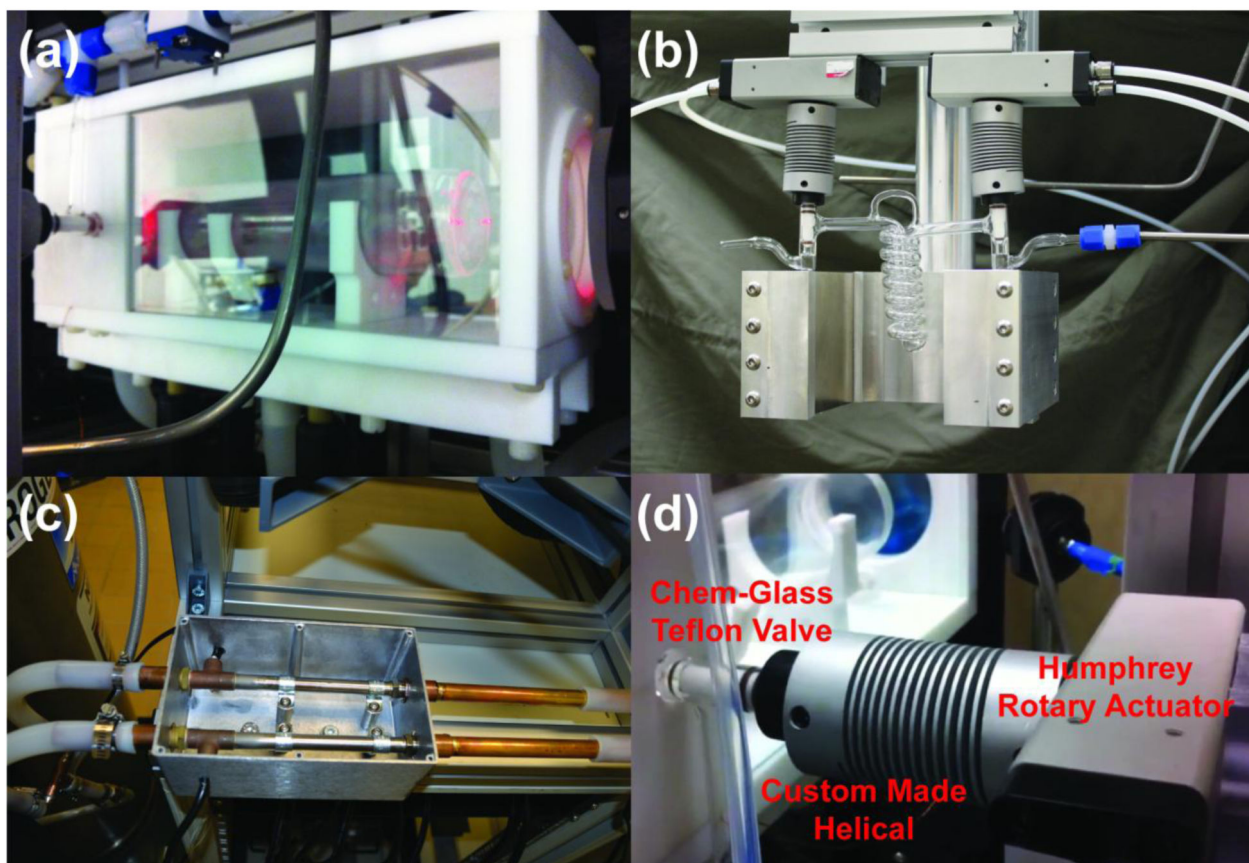


**Figure 3.**

(a) OP-Oven with OP-Cell (Mid-Rivers Glassblowing, Inc., St. Charles, MO, P/N MRG934-01A) mounted inside, with gas manifold components shown connected to the OP-Cell. (b) Glass (Pyrex) spiral storage condenser (Mid-Rivers Glassblowing, Inc., St. Charles, MO, P/N MRG927-01C) controlled via helical-rotary actuator assembly, residing in a strong (>500 Gauss) magnetic field produced by a pair of large 4 in.  $\times$  4 in.  $\times$  1 in. neodymium-iron-boride permanent magnets (Indigo Instruments). The magnet yoke was custom-machined from aluminum. (c) Two 400 W T-Type heaters (Omega Engineering, Stamford, CT) mounted inside aluminum enclosure. (d) Custom-made Helical connected and Humphrey Rotary Actuator assembly allowing automation of the Chem-Glass Teflon stopcocks. A video of the glass-valve actuation procedure can be viewed at: <http://www.youtube.com/watch?v=w33xs9KHuB0>.

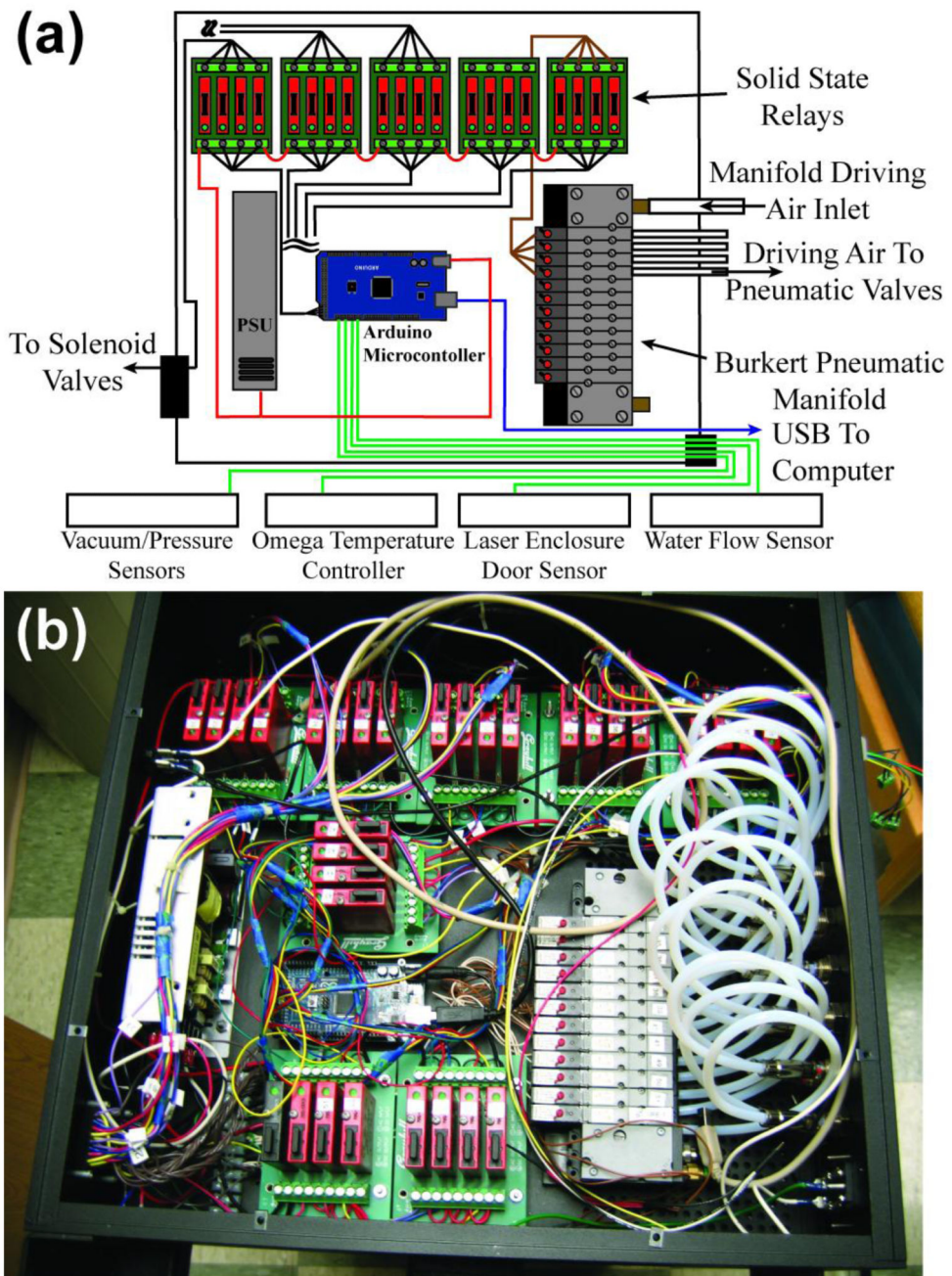


**Figure 4.**

(a) Schematic of all major components of the Microcontroller automation box. (b) Corresponding photograph.

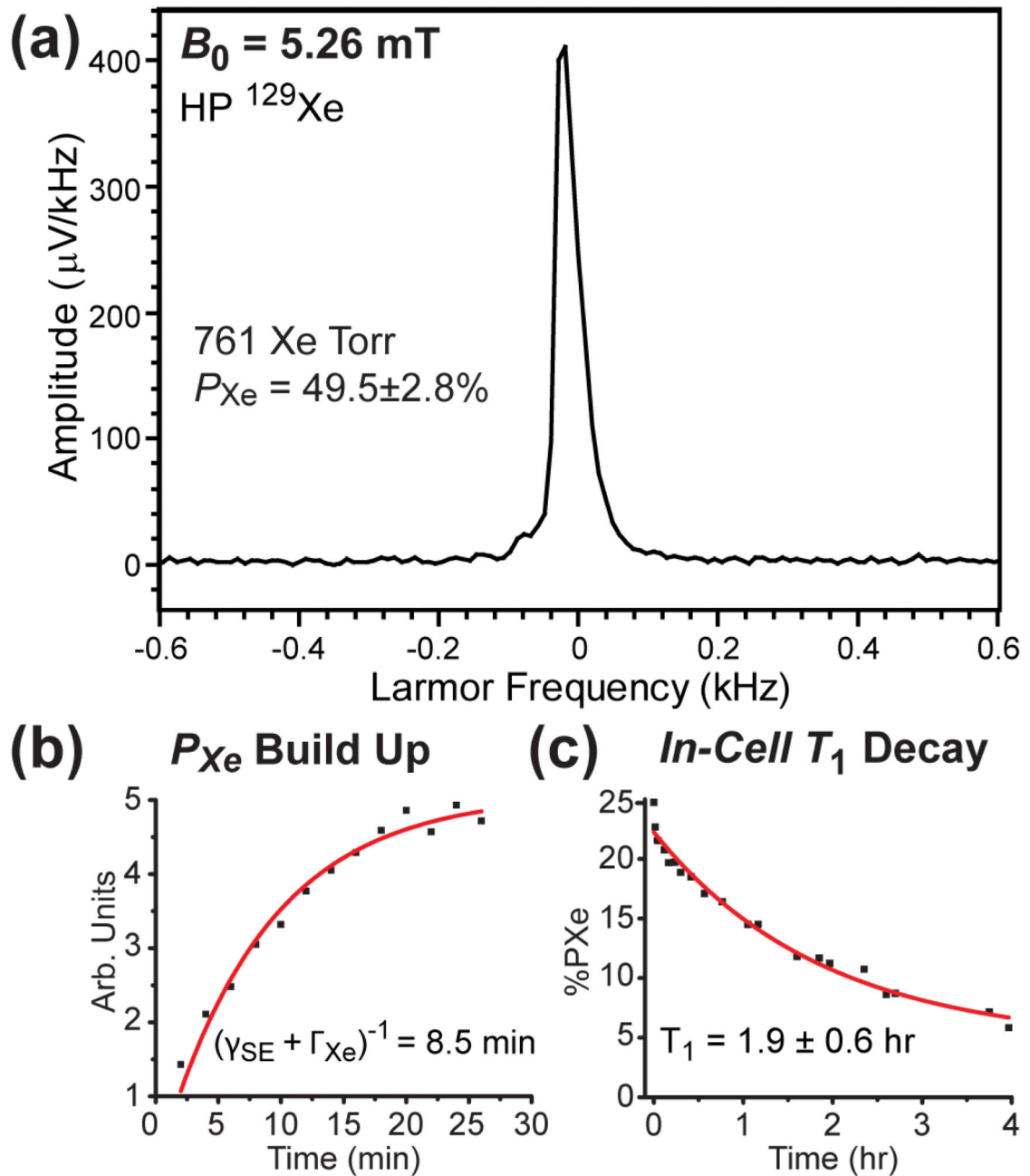
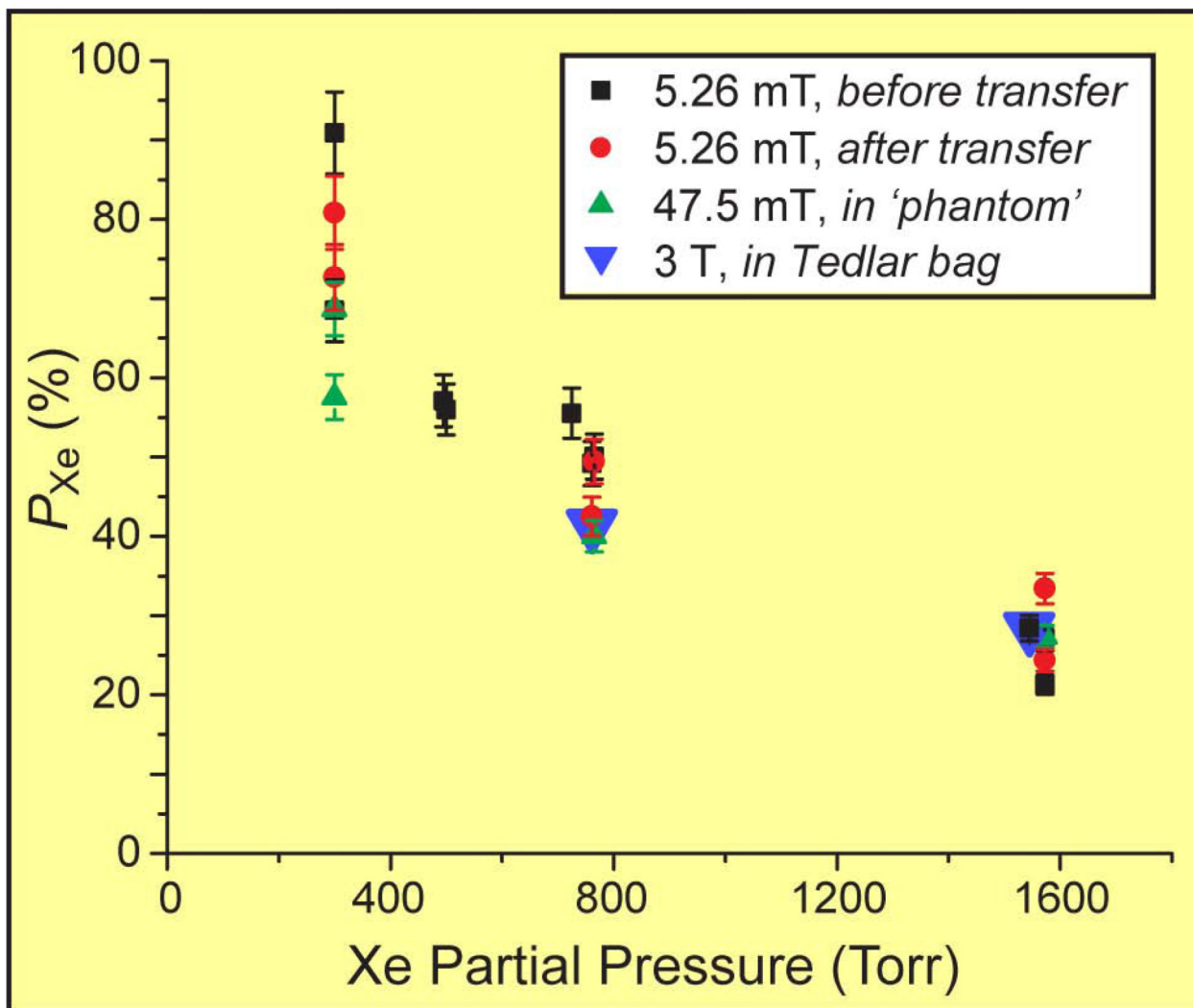


Figure 5.

(a) Example of low-field *in-situ* HP  $^{129}\text{Xe}$  NMR used for QA, here obtained from a SEOP cell containing 761 Torr Xe and 1239 Torr  $\text{N}_2$ . (b) Typical in-cell  $P_{\text{Xe}}$  build-up curve measured via *in situ*  $^{129}\text{Xe}$  NMR, here for a cell containing  $\sim 725$  Torr Xe /  $\sim 1275$  Torr  $\text{N}_2$ . (c) Spin-lattice  $T_1$  decay curve for HP  $^{129}\text{Xe}$  NMR signals from Xe gas measured at 5.26 mT of a cell containing 495 Torr Xe / 1300 Torr  $\text{N}_2$  following SEOP and subsequent cell cool-down to 33 °C (by which point the Rb should be condensed—providing a more accurate measure of the intrinsic cell relaxation rate). In normal operation, HP  $^{129}\text{Xe}$  gas is typically transferred from the OP-cell to the sample at  $\sim 40$  °C to help preserve more of the polarization.



**Figure 6.**

$^{129}\text{Xe}$  nuclear spin polarization values measured at 5.26 mT, 47.5 mT, and/or 3 T, plotted versus xenon partial pressure determined at loading (40). Labels '*before transfer*' and '*after transfer*' respectively refer to measurements obtained from Xe gas remaining within the SEOP cell before and after some of the gas was transferred to another container. Error bars are determined from the uncertainties in the spectral integral values obtained from the respective thermally-polarized reference samples. The value at 725 Torr was obtained with 82%-enriched  $^{129}\text{Xe}$  loaded with a different gas manifold.

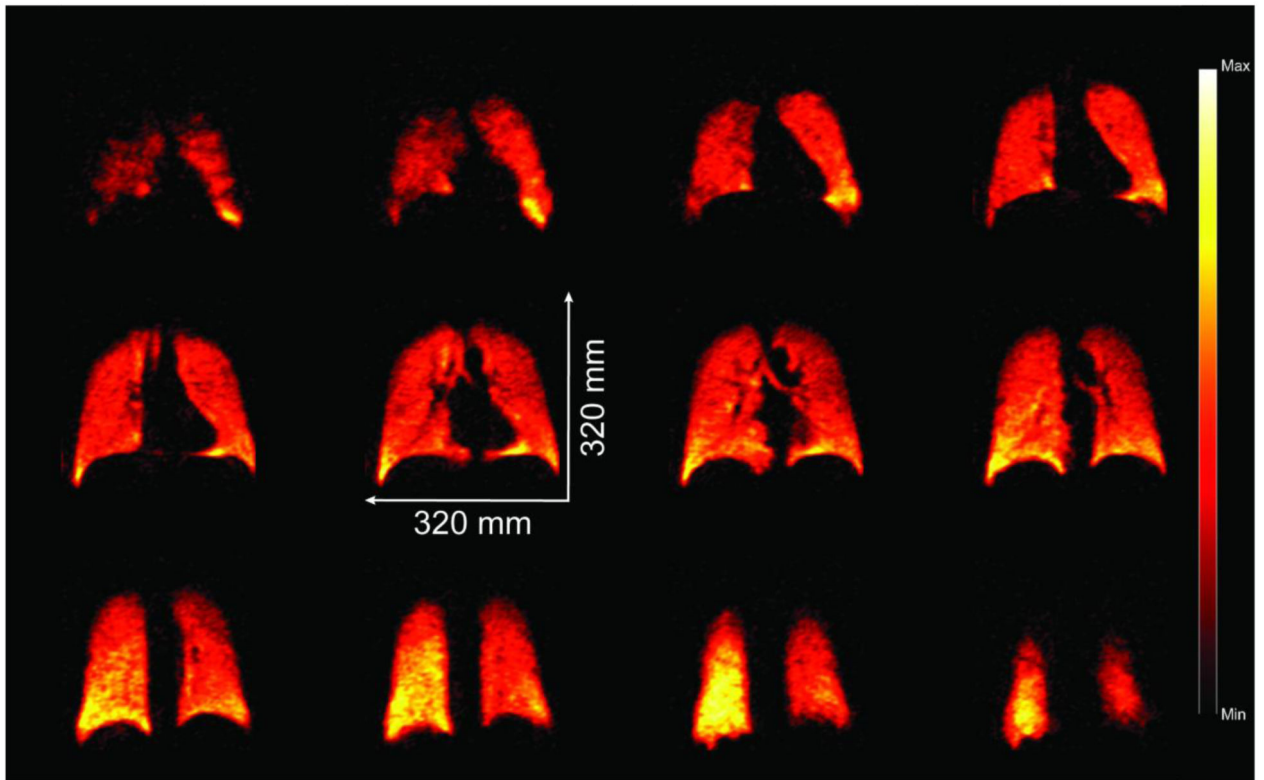


**Figure 7.**

Selected (12 of 14) false-color 2D slices from a 3D  $^{129}\text{Xe}$  GRE chest image from a healthy subject following inhalation of HP  $^{129}\text{Xe}$  prepared using the XeNA polarizer (anterior to posterior, reading left to right, top to bottom). TE/TR 1.12/11 ms (SAR-limited), tipping angle  $\alpha=6^\circ$ ,  $80\times 80\times 14$  matrix, acquisition time=4.5 s; FOV= $320\times 320\times 196$  mm<sup>3</sup>, data zero-filled to give  $2\times 2\times 14$  mm<sup>3</sup> digital resolution (SNR~8-15).